Vietnam Journal of Catalysis and Adsorption
Tạp chí xúc tác và hấp phụ Việt Nam

https://jca.edu.vn

Synthesis and Characterization of Nickel-Manganese Oxide Catalysts for the Complete Oxidation of Toluene

Nga Hang Thi Phan[1], Ngoc Nguyen Thi Tuyet[2], Minh Tuan Nguyen Dinh[2,*]

[1] *School of of Medicine and Pharmacy, The University of Da Nang, Da Nang 550000, Vietnam*
[2] *The University of Da Nang, University of Science and Technology, Da Nang 550000, Vietnam*
** Email: ndmtuan@dut.udn.vn*

ARTICLE INFO

Received: 08/01/2026
Accepted: 11/03/2026
Published: 30/03/2026

Keywords:
Binary nickel-manganese oxide; co-precipitation; complete oxidation; toluene; VOCs

ABSTRACT

Binary nickel–manganese oxide catalysts were synthesized via a co-precipitation method and evaluated for the complete oxidation of toluene, a representative volatile organic compound (VOCs). The structural, morphological, textural, and redox properties of the catalysts were systematically characterized by X-ray diffraction (XRD), scanning electron microscopy (SEM), nitrogen adsorption–desorption isotherms, and H_2 temperature-programmed reduction (H_2-TPR). The nickel manganese oxide catalysts exhibit multiphase structures mainly composed of MnO_2, $NiMnO_3$, $NiMn_2O_4$, and Mn-doped NiO, along with a significantly higher specific surface area and pore volume compared to MnO_x and NiO. Catalytic tests demonstrate that the $NiMn_2O_x$ catalyst shows superior activity, achieving complete oxidation of toluene at 273 °C and exhibiting the lowest T_{50} and T_{90} values (237 °C and 248 °C, respectively) among the tested catalysts. The enhanced catalytic performance is attributed to the synergistic interaction between Ni and Mn species, which induces lattice distortion and enhances reducibility. These results highlight the potential of binary Ni–Mn oxide composite catalyst as an efficient and cost-effective material for VOCs abatement.

Introduction

Volatile organic compounds (VOCs), such as toluene, xylene, and benzene, are hazardous air pollutants emitted from numerous industrial activities including painting, printing, petroleum refining, petrochemical processing, and vehicle exhaust [1]. Their high toxicity, persistence, and contribution to photochemical smog necessitate the development of effective strategies for their complete removal. Among available technologies, catalytic total oxidation has been widely accepted as one of the most efficient and environmentally friendly methods, converting VOCs completely into CO_2 and H_2O at moderate temperatures [2, 3].

Over the past decades, various types of catalysts have been developed for VOCs oxidation, including noble metal-based catalysts (e.g., Pt, Pd, Au), which exhibit excellent activity and low light-off temperatures [3]. However, their high cost and susceptibility to poisoning by water or sulfur compounds have limited large-scale applications. As an alternative, transition metal oxides have emerged as cost-effective and thermally stable catalysts. Among them, manganese oxides (MnO_x) are extensively studied due to their multiple oxidation states (Mn^{2+}, Mn^{3+}, Mn^{4+}), abundant oxygen vacancies, and strong redox properties [4–7] Nevertheless, the standalone MnO_x often suffers from poor low-temperature activity and limited durability [3, 8].

https://doi.org/10.62239/jca.2026.007
50

©2026 by the authors. Licensee Vietnam Journal of Catalysis and Adsorption. This article is an open access article distributed under the terms and conditions of the Creative Commons Attribution (CC BY) license (https://creativecommons.org/licenses/by/4.0/).

To enhance catalytic performance, binary metal oxides have been investigated to harness synergistic effects between different cations [9, 10]. In this context, the binary oxide between manganese and other transitional metal (Cu, Co…) have shown promising activity for the total oxidation of toluene [11–14]. The introduction of other metal into the MnO_x lattice or the synergistic effect between the two metal oxides can modify the electronic structure, increase the number of active oxygen species, and improve catalytic performance [11,13,14]. Several studies have reported that Cu–MnO_x, $CuMn_2O_4$, Co-Mn, Ni-Mn catalysts exhibit high catalytic activity and enhanced CO_2 selectivity compared to single-component oxides [14–19].

Among the binary oxides, nickel-manganese oxide catalysts have been shown to exhibit excellent catalytic activity and stability in total oxidation of benzene [19]. As shown by Tang et al. [19], the catalytic performance of the binary catalyst can be attributed to their higher content of surface-adsorbed oxygen species and better low-temperature reducibility. However, this kind of catalyst has not been studied for toluene removal. As a matter of fact, the catalytic performance of the catalysts largely depends on the synthesis method and type of VOCs. Hence, the study on the binary nickel-manganese oxide for the complete oxidation of VOCs is necessary.

In this study, we synthesized nickel manganese oxide catalysts using a facile co-precipitation method followed by thermal treatment. The catalysts were thoroughly characterized by XRD, SEM, H_2-TPR and N_2 adsorption–desorption techniques to investigate their phase composition, morphology, reducibility and textural properties. The catalytic performance for the complete oxidation of toluene was systematically evaluated and compared with that of the individual NiO and MnO_x catalysts.

Experimental

$Ni(NO_3)_2.6H_2O$ (≥97%) and $Mn(NO_3)_2$ (≥97%) were purchased from Sigma Aldrich. NaOH (>96%) was obtained from Xilong Chemical. Toluene (>99.5%) was purchased from Merck. All chemicals were used as received without further treatment.

Methods

Two nickel–manganese oxide catalysts were synthesized by a co-precipitation method with Ni/Mn molar ratios of 1 and 2. Typically, 15 mL of 0.25 M $Mn(NO_3)_2$ and 15 mL of 0.25 M $Ni(NO_3)_2$ solutions were mixed and stirred in a beaker. Subsequently, 65 mL of 0.5 M NaOH solution was added dropwise under continuous stirring. The mixture was further stirred for 30 minutes, after which the resulting suspension was transferred to a flask placed in an oil bath at 95 °C and connected to a vacuum rotator. After complete evaporation of water, the obtained solid was dried at 110 °C for 12 hours, followed by heat treatment at 220 °C for 2 hours to ensure complete decomposition of nitrate species. Finally, the sample was calcined at 400 °C for 4 hours. The resulting catalyst was denoted as $NiMnO_x$. The $NiMn_2O_x$ sample was prepared using the same procedure, except that the amount of $Mn(NO_3)_2$ was doubled. Single-component NiO and MnO_x catalysts were synthesized following the same procedure, while omitting the manganese or nickel precursor, respectively.

Several key physicochemical properties, including phase composition, microstructural morphology, and textural characteristics (such as specific surface area, pore volume, and pore size distribution), were determined using various techniques. X-ray diffraction (XRD) analysis was performed using a SmartLab diffractometer (Rigaku) to identify the crystalline phases. Scanning electron microscopy (SEM) was conducted on a JEOL JSM-6020LV instrument to examine surface morphology. Nitrogen adsorption–desorption isotherms were measured at 77 K using a Micromeritics ASAP 2020 apparatus to evaluate the textural properties.

The catalytic activity was evaluated in a fixed-bed quartz microreactor with an inner diameter of 6 mm, as previously reported [20]. In a typical experiment, 100 mg of catalyst was placed on a quartz wool plug inside the reactor. A thermocouple inserted into the catalyst bed was used to monitor the reaction temperature in real time. The feed gas contained 1000 ppm of toluene diluted in synthetic air, with a total flow rate of 100 $mL{\cdot}min^{-1}$, resulting in a gas hourly space velocity (GHSV) of approximately 60,000 mL/g/h. The toluene vapor was generated by passing a nitrogen stream through a saturator containing liquid toluene maintained at 5 °C. The resulting toluene-containing gas was then diluted with a stream of dry air to obtain the desired toluene concentration and total flow rate. The reactant and product gases were continuously analyzed using an online gas chromatograph (Agilent 7890B) equipped with a flame ionization detector (FID) for toluene detection and a thermal conductivity detector (TCD) for CO_2 and other permanent gases. Toluene conversion to CO_2 was calculated according to the following equation.

https://doi.org/10.62239/jca.2025.007

$$\eta_{C_7H_8} = \frac{[CO_2]_{out}}{7 \times [C_7H_8]_{in}} \times 100$$

where $[C_7H_8]_{in}$ and $[CO_2]_{out}$ signify the concentration of toluene in feed and CO_2 in the outlet gas streams, respectively.

Results and discussion

The crystalline phases of the nickel–manganese oxides were identified by X-ray diffraction. As shown in Figure 1, all diffraction peaks of the MnO_x and NiO samples can be indexed to Mn_5O_8 (ICDD PDF No. 01-072-1427) and the bunsenite phase of NiO, respectively. For the NiO sample, the characteristic diffraction peaks at 2θ = 37.3° and 43.3° correspond to the (111) and (200) crystallographic planes of bunsenite NiO.

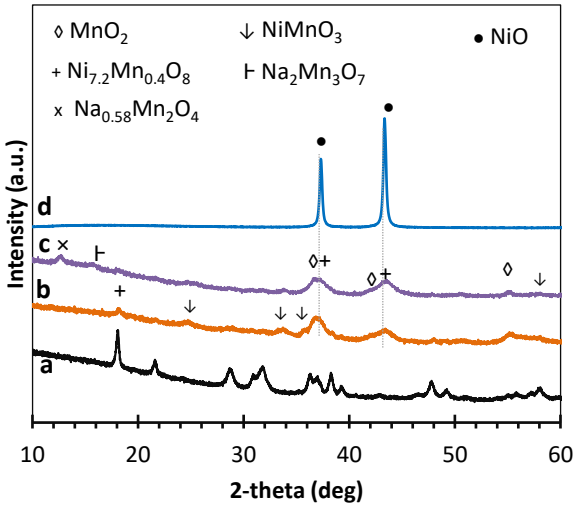

Fig. 1: XRD pattern of a) MnO_x, b) $NiMn_2O_x$, c) $NiMnO_x$ and d) NiO catalysts

In contrast, the XRD pattern of the $NiMn_2O_x$ sample reveals the coexistence of several crystalline phases, including MnO_2, $NiMnO_3$, and $Ni_{7.2}Mn_{0.4}O_8$. The diffraction peaks observed at 2θ = 24.7°, 33.8°, 36.6°, 41.9°, 50.6°, and 55.2° are assigned to the $NiMnO_3$ phase (ICDD PDF No. 01-075-2089). The presence of MnO_2 is confirmed by diffraction peaks at 2θ = 36.7° and 42.3° (ICDD PDF No. 00-030-0830). In addition, the peaks at 2θ = 37.3° and 43.5° can be attributed to the $Ni_{7.2}Mn_{0.4}O_8$ phase (ICDD PDF No. 01-089-5879), which originates from the incorporation of Mn ions into the NiO lattice. Compared to the pure NiO sample, the (200) diffraction peak shifts toward a higher 2θ angle (43.5°), indicating lattice contraction induced by the substitution of Ni^{2+} ions with Mn^{3+}/Mn^{4+} ions. This lattice distortion can enhance the formation of defects and improve oxygen mobility in the nickel–manganese oxide composite catalyst, which is beneficial for the catalytic oxidation of toluene [2], 15].

Furthermore, the XRD pattern of the $NiMnO_x$ sample also shows the formation of the $NiMn_2O_4$ spinel phase, along with sodium-containing manganese oxides such as $Na_{0.58}Mn_2O_4$ (ICDD PDF No. 01-073-9669) and $Na_2Mn_3O_7$ (ICDD PDF No. 01-070-7202), likely originating from residual sodium species introduced during the synthesis process.

The morphology of MnO_x, $NiMn_2O_x$, and NiO, catalysts are examined by using SEM technique, as depicted in Figure 2. The SEM images of MnO_x and NiO (Figures 2A, B and E) reveal the formation of nanoparticles ranging from several dozen to hundred nanometers in size with some octahedra NiO particles. In contrast, the morphology of $NiMn_2O_x$ oxide consists of much smaller nanoparticles (Figure 2C and D). The smaller particle size of $NiMn_2O_x$ is expected to result in a larger specific surface area, as the surface-to-volume ratio increases with decreasing particle size. This provides more accessible active sites for the catalytic oxidation of toluene.

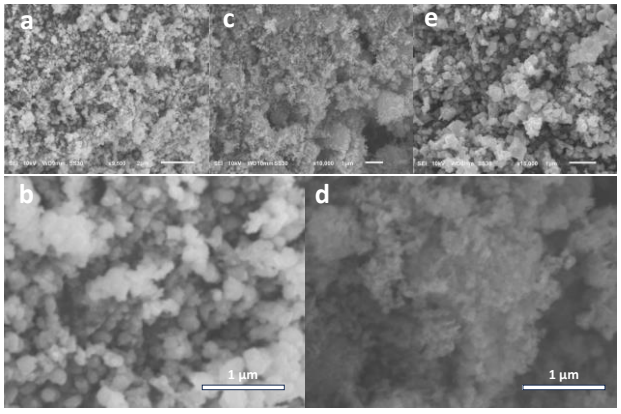

Fig. 2: SEM images of a, b) MnO_x, c,d) $NiMn_2O_x$, and e) NiO

The textural properties, including BET surface area, pore volume, and pore size distribution, were determined by nitrogen adsorption–desorption isotherms at 77 K. As shown in Figures 3A and B, all catalysts exhibit type IV isotherms with hysteresis loops, indicating the presence of mesoporous structures. The width and shape of the hysteresis loops provide insight into the pore size distribution of the samples. For the MnO_x sample, a narrow hysteresis loop observed in the P/P_0 range of 0.9–1.0 suggests a relatively uniform mesoporous structure with a narrow pore size distribution, mainly below 6 nm (Figures 3C). In contrast, the NiO sample exhibits a broader hysteresis loop spanning from P/P_0 = 0.84 to 1.0, indicating a

https://doi.org/10.62239/jca.2026.007

wider pore size distribution that includes mesopores of 3–5 nm as well as macropores in the range of 100–400 nm. The $NiMnO_x$ sample shows a hysteresis loop with a similar shape but with a narrower pore size distribution centered around approximately 200 nm (Figures 3D). Meanwhile, the $NiMn_2O_x$ sample displays a more extended hysteresis loop over the P/P_0 range of 0.75–1.0, indicating a more developed mesoporous structure. Its pore size distribution ranges from 6 to 45 nm, with a prominent maximum at around 9 nm. The BET surface area and pore volume of the $NiMn_2O_x$ catalyst are 65 $m^2\ g^{-1}$ and 0.34 $cm^3\ g^{-1}$, respectively, which are significantly higher than those of the $NiMnO_x$ catalyst (40 $m^2\ g^{-1}$ and 0.30 $cm^3\ g^{-1}$) and the single metal oxides (20 $m^2\ g^{-1}$ and 0.07 $cm^3\ g^{-1}$ for MnO_x, and 59 $m^2\ g^{-1}$ and 0.09 $cm^3\ g^{-1}$ for NiO). The presence of internal porous structures within the nanoparticles contributes to the enhanced BET surface area. The increased surface area and pore volume of $NiMn_2O_x$ provide a greater number of accessible active sites, which are largely located within the porous framework, thereby favoring the complete oxidation of toluene.

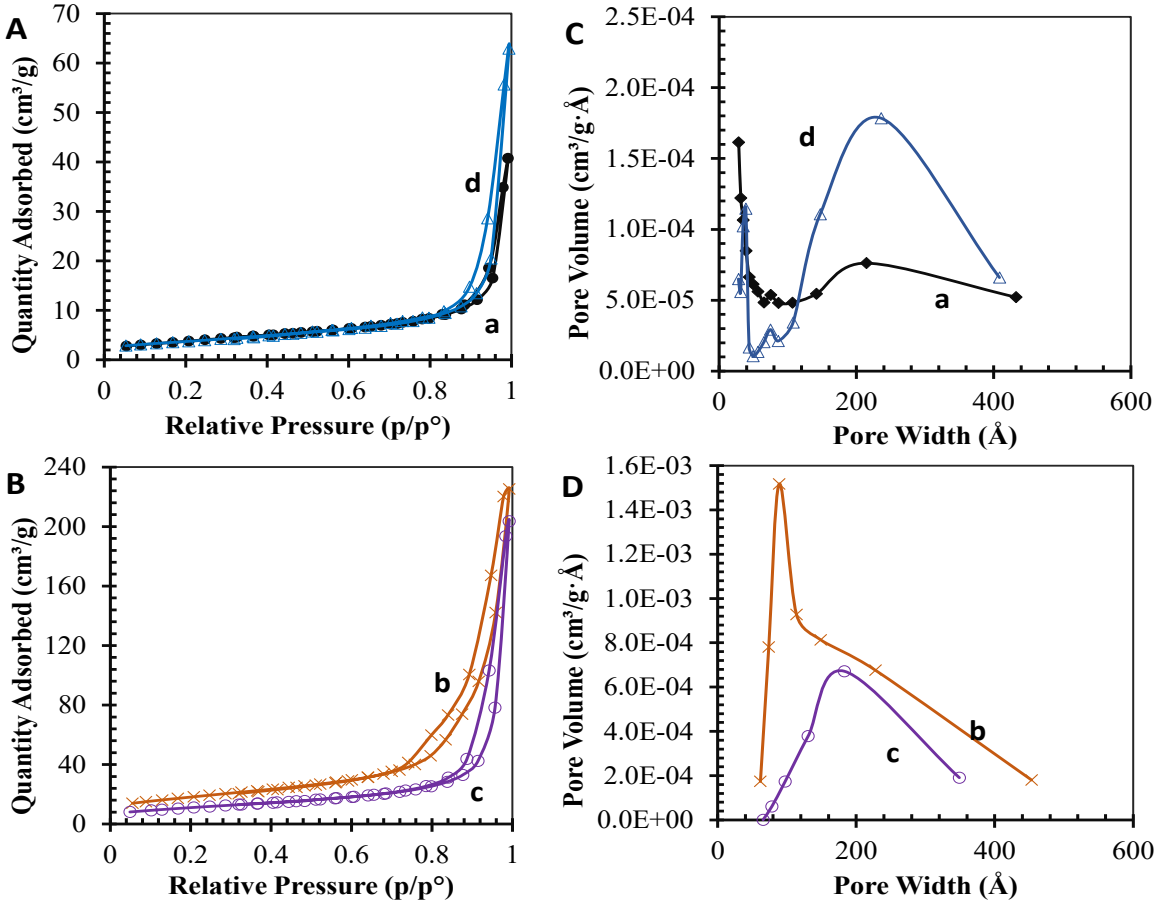

Fig. 3: (A, B) Adsorption-desorption isotherm; and (C, D) pore size distribution of a) MnOx, b) $NiMnO_x$, c) $NiMn_2O_x$ and d) NiO

The H_2-TPR profiles of MnO_x, $NiMnO_x$, and $NiMn_2O_x$ are presented in Figure 4, revealing distinct differences in reducibility induced by nickel incorporation. The MnO_x sample exhibits two reduction peaks in the temperature range of approximately 250–450 °C, which are characteristic of stepwise reduction processes involving Mn species [16]. The lower-temperature peak is commonly attributed to the reduction of surface or near-surface Mn^{4+} species to Mn^{3+}, while the higher-temperature peak corresponds to the further reduction of bulk Mn^{3+} to Mn^{2+}, associated with the removal of lattice oxygen. In contrast, the $NiMnO_x$ catalyst shows a noticeable shift of the reduction peaks toward lower temperatures along with peak broadening, indicating enhanced reducibility compared to MnO_x. This behavior suggests a strong interaction between Ni and Mn species, which weakens the metal–oxygen bonds and facilitates the removal of lattice oxygen. The broadened reduction feature also reflects the presence of multiple reducible species and heterogeneous redox environments arising from the formation of mixed Ni–Mn oxide phases and interfacial regions.

https://doi.org/10.62239/jca.2025.007

Table 1: Textural properties and catalytic performance of the catalysts

Catalyst	S_{BET} (m^2/g)	V_P (cm^3/g)	$n(H_2)$ (mmol/g)	Catalytic performances (°C)		
				T_{10}	T_{50}	T_{90}
MnO_x	20	0.07	7.1	230	289	326
$NiMn_2O_x$	65	0.34	8.7	212	237	248
$NiMnO_x$	40	0.30	8.0	208	245	314
NiO	59	0.09	-	286	354	>400

$n(H_2)$: hydrogen consumption

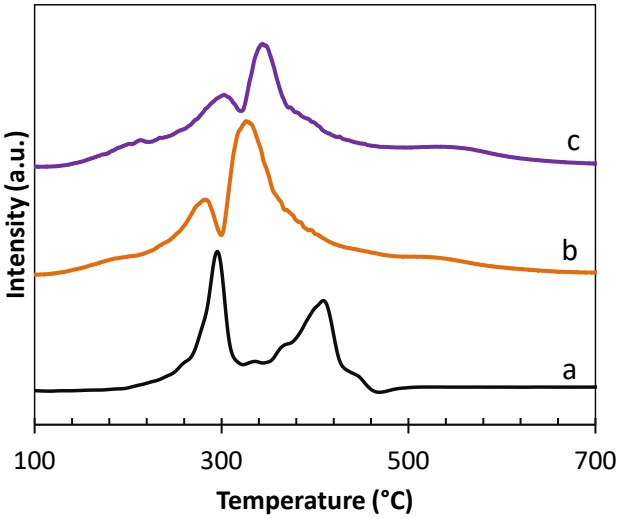

Fig. 4: H_2-TPR profiles a) MnOx, b) $NiMn_2O_x$, and c) $NiMnO_x$

The $NiMn_2O_x$ sample exhibits the most pronounced low-temperature reduction feature among the three catalysts, with a dominant peak appearing at lower temperatures and an extended reduction profile (Fig. 4, line b). This indicates a higher proportion of readily reducible oxygen species and improved redox capability. In addition to the peak shift, the total hydrogen consumption further confirms the enhanced redox properties of the Ni-containing catalysts. The H_2 uptake increases from 7.11 mmol/g for MnO_x to 7.99 mmol/g for $NiMnO_x$ and 8.70 mmol/g for $NiMn_2O_x$, corresponding to approximately 12% and 22% increases, respectively. The higher hydrogen consumption indicates a greater amount of reducible oxygen species and improved redox capacity [21]. The $NiMn_2O_x$ catalyst, exhibiting both the lowest reduction temperature and the highest H_2 uptake, demonstrates the strongest reducibility among the samples. Such enhanced reducibility and oxygen mobility are highly favorable for catalytic oxidation reactions following a Mars–van Krevelen mechanism [2, 3].

The catalytic performance of the nickel–manganese oxide catalysts for the complete oxidation of toluene to CO_2 was evaluated in a gas-phase fixed-bed reactor using a feed stream containing 1000 ppm toluene at a gas hourly space velocity (GHSV) of 60,000 mL/g/h. The conversion of toluene over the nickel–manganese mixed oxides and the single metal oxide catalysts was plotted as a function of catalyst temperature, yielding the so-called light-off curves, as shown in Figure 5. At temperatures below 190 °C, the conversion of toluene was negligible for all catalysts. From 220 °C onward, the conversion over the $NiMn_2O_x$ catalyst increased sharply, reaching 90% at 248 °C and gradually approaching complete conversion at 273 °C. No other organic by-products or CO were detected throughout the reaction, indicating high selectivity toward CO_2 formation.

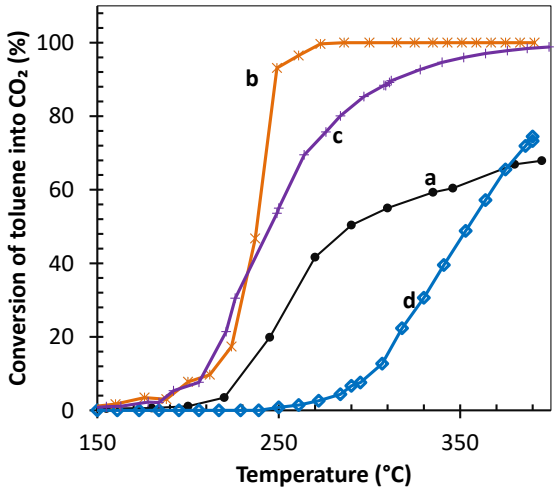

Fig. 5: Catalytic performance of a) MnO_x, b) $NiMnO_x$, c) $NiMn_2O_x$ and d) NiO catalysts with an inlet toluene concentration of 1000 ppm

The light-off curves of the $NiMnO_x$ and $NiMn_2O_x$ catalysts were significantly shifted toward lower temperatures compared with those of the MnO_x and NiO catalysts, demonstrating their superior low-temperature catalytic activity. The catalytic performance was further quantified using the characteristic temperatures T_{10}, T_{50}, and T_{90}, corresponding to 10%, 50%, and 90% conversion of toluene to CO_2, respectively, as summarized in Table 1. Among all tested catalysts, $NiMn_2O_x$ exhibited the lowest T_{50} and T_{90} values, at 237 °C and 248 °C, respectively, further confirming its superior catalytic efficiency for the complete oxidation of toluene.

As summarized in Table 2 and compared with the data reported in litterature, the $NiMn_2O_x$ catalyst exhibits catalytic performance comparable to several transition-metal oxide systems for toluene oxidation. Although

https://doi.org/10.62239/jca.2026.007

some MnO_2 polymorphs or noble metal catalysts exhibit slightly lower light-off temperatures, these performances are generally achieved under much lower space velocities or lower inlet toluene concentrations. In contrast, the $NiMn_2O_x$ catalyst developed in this work reaches T_{90} at 248 °C under a relatively high GHSV of 60,000 h^{-1}, demonstrating competitive activity under more demanding reaction conditions.

Table 2: Comparison of catalytic performance for the complete oxidation of toluene.

Catalyst	T_{90} (°C)	Toluene (ppm)	GHSV (mL/g/h)	Ref
$NiMn_2O_x$	**248**	1000	60,000	This work
MnO_2	290	5000	10,000	[9]
α-MnO_2	238	1000	20,000	[22]
α-MnO_2	255	1000	60,000	[23]
β-MnO_2	295	1000	60,000	[24]
1 wt.% Pt/Al_2O_3	235	600	80,000	[25]
1 wt.% Pd/Al_2O_3	190 °C	1000	15,000	[26]
Co_3O_4	260	1000	20,000	[27]
$CuMnO_x$	240	5000	15,000	[10]

The enhanced catalytic activity of the nickel–manganese oxide catalysts can be well correlated with their structural, textural, and redox properties revealed by XRD, N_2 adsorption–desorption, and H_2-TPR analyses. XRD analysis reveals lattice distortion and the formation of mixed Ni–Mn oxide phases, which favor the generation of catalytic defects. BET results show that $NiMn_2O_x$ possesses a higher surface area and pore volume, providing more accessible active sites and improved mass transfer. Although $NiMnO_x$ exhibits a lower BET surface area than NiO, its superior catalytic activity indicates that surface area is not the dominant factor controlling the reaction rate. Instead, the enhanced performance of $NiMnO_x$ can be attributed to strong Ni–Mn synergistic interactions arising from the formation of mixed oxide phases and interfacial structures [28]. These interactions promote oxygen vacancy generation and improve lattice oxygen mobility, as evidenced by the shift of reduction peaks toward lower temperatures and the increased hydrogen consumption observed in the H_2-TPR analysis. The combination of these features promotes efficient lattice oxygen participation in the reaction, accounting for the lower light-off temperatures and enhanced activity of $NiMn_2O_x$ in the complete oxidation of toluene.

Conclusion

In summary, the binary nickel-manganese catalysts consisting of multi oxides including MnO_2, $NiMnO_3$, $NiMn_2O_4$, and Mn-doped NiO phases were successfully synthesized by co-precipitation method. These catalysts exhibited superior catalytic performance for the complete oxidation of toluene compared with the single-component MnO_x and NiO catalysts. The $NiMn_2O_x$ catalyst reached complete conversion of 1000 ppm of toluene at 273 °C, with the lowest T_{50} (237 °C) and T_{90} (248 °C) among the tested catalysts. The remarkable activity enhancement may be attributed to the synergistic interaction between Ni and Mn species. These findings suggest that $NiMn_2O_x$ is a promising catalyst for the abatement of VOCs such as toluene through catalytic total oxidation.

Acknowledgments

This word is funded by the Vietnam National Foundation for Science and Technology Development (NAFOSTED) under grant number 104.05-2021.37.

References

1. C. He, J. Cheng, X. Zhang, M. Douthwaite, S. Pattisson, Z. Hao, Chem. Rev., 119(7) (2019) 4471–4568. https://doi.org/10.1021/acs.chemrev.8b00408
2. H. Huang, Y. Xu, Q. Feng, D.Y.C. Leung, Catal. Sci. Technol., 5(5) (2015) 2649–2669. https://doi.org/10.1039/C4CY01733A
3. Y. Lyu, C. Li, X. Du, Y. Zhu, Y. Zhang, S. Li, Environ. Sci. Pollut. Res., 27(3) (2020) 2482–2501. https://doi.org/10.1007/s11356-019-07037-2
4. J. Li, H. Liu, Y. Deng, G. Liu, Y. Chen, J. Yang, Nanotechnol. Rev., 5(1) (2016) 3–15. https://doi.org/10.1515/ntrev-2015-0051
5. M.T. Phan, T.H.N. Chu, D. Nguyen, Vietnam J. Catal. Adsorpt., 9(1) (2020) 88–92.
6. M.T. Phan, M.D. Nguyen, D. Nguyen, Univ. Danang - J. Sci. Technol., 122(1) (2018) 11–15.
7. T.T.H. Tran, T.T. Le, L.B. Thuy, P.T.M. Phuong, L.M. Thang, Vietnam J. Catal. Adsorpt., 12(2) (2023) 110–115. https://doi.org/10.51316/jca.2023.039
8. R. Liu, H. Guo, Z. Yang, Y. Liu, X. Zhao, X. Wu, Z. Zhang, Catal. Sci. Technol., 12(23) (2022) 6945–6991. https://doi.org/10.1039/D2CY01181F
9. M.T. Le, P.A. Nguyen, T.T.H. Tran, T.H.N. Chu, Y. Wang, H. Arandiyan, Top. Catal., 66(1–4) (2023) 117–125. https://doi.org/10.1007/s11244-022-01676-5

10. T.T.H. Tran, L.B. Thuy, P.T.M. Phuong, L.M. Thang, Vietnam J. Catal. Adsorpt., 10(4) (2021) 56–62. https://doi.org/10.51316/jca.2021.068
11. M.T. Nguyen Dinh, C.C. Nguyen, S.S. Lin, T.L. Truong Vu, V.T. Ho, Y. Wang, H. Arandiyan, Q.D. Truong, Ind. Eng. Chem. Res., 62(18) (2023) 6908–6919. https://doi.org/10.1021/acs.iecr.3c00196
12. Z.Y. Tian, P.H.T. Ngamou, V. Vannier, K. Kohse-Höinghaus, N. Bahlawane, Appl. Catal. B Environ., 117–118 (2012) 125–134. https://doi.org/10.1016/j.apcatb.2012.01.013
13. Y. Wang, D. Yang, S. Li, L. Zhang, G. Zheng, L. Guo, Chem. Eng. J., 357 (2019) 258–268. https://doi.org/10.1016/j.cej.2018.09.156
14. Z. Hu, J.Y. Lee, X. Wang, G. Sun, S.H. Choi, J.S. Kim, Y.S. Kim, S.D. Kim, Ind. Eng. Chem. Res., 61(14) (2022) 4803–4815. https://doi.org/10.1021/acs.iecr.1c05077
15. S.M. Saqer, D.I. Kondarides, X.E. Verykios, Appl. Catal. B Environ., 103(3–4) (2011) 275–286. https://doi.org/10.1016/j.apcatb.2011.01.001
16. Z. Ye, J. Giraudon, N. Nuns, P. Simon, A. De Geyter, J.F. Lamonier, Appl. Catal. B Environ., 223 (2018) 154–166. https://doi.org/10.1016/j.apcatb.2017.06.072
17. C.W. Ahn, J.R. Kim, S.K. Ihm, J. Ind. Eng. Chem., 47 (2017) 439–445. https://doi.org/10.1016/j.jiec.2016.12.018
18. M.R. Morales, B.P. Barbero, L.E. Cadús, Appl. Catal. B Environ., 74(1–2) (2007) 1–10. https://doi.org/10.1016/j.apcatb.2007.01.008
19. W. Tang, X. Wu, S. Liu, D. Li, Z. Zhao, B. Chen, Y. Chen, Catal. Sci. Technol., 6(6) (2016) 1710–1718. https://doi.org/10.1039/C5CY01119A
20. M.T. Nguyen Dinh, C.C. Nguyen, T.L.T. Vu, V.T. Ho, Q.D. Truong, Appl. Catal. A Gen., 595 (2020) 117473. https://doi.org/10.1016/j.apcata.2020.117473
21. C. Zhang, J. Deng, J. Xie, K. Xie, S.S.A. Shah, S. Chen, ChemCatChem, 12(13) (2020) 3512–3522. https://doi.org/10.1002/cctc.202000449
22. F. Shi, S. Cao, C. Sun, J. Yang, M. Chen, Appl. Catal. A Gen., 433–434 (2012) 206–213. https://doi.org/10.1016/j.apcata.2012.05.016
23. X. Zhang, G. Zhang, H. He, J. Li, J. Cheng, Appl. Surf. Sci., 493 (2019) 9–17. https://doi.org/10.1016/j.apsusc.2019.06.255
24. P. Gong, F. He, J. Xie, D. Fang, Chemosphere, 318 (2023) 137938. https://doi.org/10.1016/j.chemosphere.2023.137938
25. Z. Zhang, Z. Jiang, W. Shangguan, Catal. Today, 264 (2016) 270–278. https://doi.org/10.1016/j.cattod.2015.10.040
26. S.C. Kim, W.G. Shim, Appl. Catal. B Environ., 92(3–4) (2009) 429–436. https://doi.org/10.1016/j.apcatb.2009.09.001
27. G. Bai, N. Dai, J. Yang, S. Liu, T. Fang, Appl. Catal. A Gen., 450 (2013) 42–49. https://doi.org/10.1016/j.apcata.2012.09.054
28. L. Chen, J. Yang, S. Liu, T. Fang, C. Xu, Q. Zhu, Chem. Eng. J., 369 (2019) 1129–1137. https://doi.org/10.1016/j.cej.2019.03.142